Mimicking mergers: mistaking black hole captures as mergers

Weichangfeng Guo [ID],[1]★ Daniel Williams [ID],[2]★ Ik Siong Heng [ID],[2] Hunter Gabbard [ID],[2] Yeong-Bok Bae [ID],[3] Gungwon Kang [ID][4] and Zong-Hong Zhu [ID][1,5]

[1]*Department of Astronomy, Beijing Normal University, Beijing 100875, China*
[2]*SUPA, School of Physics and Astronomy, University of Glasgow, Glasgow G12 8QQ, UK*
[3]*Center for Theoretical Physics of the Universe, Institute for Basic Science (IBS), Daejeon 34126, Korea*
[4]*Department of Physics, Chung-Ang University, Seoul 06974, Korea*
[5]*School of Physics and Technology, Wuhan University, Wuhan 430072, China*

ABSTRACT

As the number of gravitational wave observations has increased in recent years, the variety of sources has broadened. Here, we investigate whether it is possible for the current generation of detectors to distinguish between very short-lived gravitational wave signals from mergers between high-mass black holes and the signal produced by a close encounter between two black holes, which results in gravitational capture and ultimately a merger. We compare the posterior probability distributions produced by analysing simulated signals from both types of progenitor events, both under ideal and realistic scenarios. We show that while under ideal conditions it is possible to distinguish both progenitors, under realistic conditions they are indistinguishable. This has important implications for the interpretation of such short signals, and we therefore advocate that these signals be the focus of additional investigation even when satisfactory results have been achieved from standard analyses.

Key words: black hole physics – gravitational waves – galaxies: nuclei.

1 INTRODUCTION

In recent years, binary black hole (BBH) observations have become a mainstay of gravitational wave (GW; Sathyaprakash & Schutz 2009) detection (Abbott et al. 2019a; Abbott et al. 2021; Collaboration et al. 2021). Observable BBH signals are produced during the late stages of the decay of a bound orbit of two black holes (BHs): these observations are typically short-lived, and have a distinctive morphology, produced by the final orbits (the 'inspiral' phase), the merger of the two BHs, and finally the 'ringdown' of the final, merged BH. Most BBHs are expected to be circularized before the merging due to the loss of the orbital energies during the inspiral phase (Peters 1964; Hinder et al. 2008; Abadie et al. 2010), therefore the current analyses of GW data and the parameter estimations of GW sources have focused on binaries with circular orbits. Eccentricity has not been detected (Romero-Shaw, Lasky & Thrane 2019; Abbott et al. 2019b; Wu, Cao & Zhu 2020) in the O1 and O2 observing runs of LIGO/Virgo (Acernese et al. 2014; Aasi et al. 2015), while a high-mass BBH event in O3a, GW190521 (Abbott et al. 2020a,b), shows evidence it may have been both highly eccentric and dynamically formed, as a result of parameter estimation analysis (Romero-Shaw et al. 2020b; Gamba et al. 2021) using both spin-aligned eccentric waveform approximants, SEOBNRE (Cao & Han 2017; Liu, Cao & Shao 2020; Romero-Shaw et al. 2020b) and TEOBResumS (Gamba et al. 2021; Nagar et al. 2021); and numerical relativity simulations (Gayathri et al. 2022).

There are several dynamical-formation scenarios (Lightman & Shapiro 1978; Sigurdsson & Hernquist 1993; Zwart & McMillan 2000; Samsing, MacLeod & Ramirez-Ruiz 2014; Morscher et al. 2015; Gondán et al. 2018; Yang et al. 2019) that support the formation and merger of binary systems while retaining eccentricity throughout their lifetime. One of the formation processes of these eccentric BH binaries is a gravitational radiation-driven capture. Captures are expected to take place in galactic nuclei, where the central super massive BH creates a steep density cusp of stellar-mass BHs. This can provide a suitable environment for eccentric BBH formation (O'Leary, Kocsis & Loeb 2009). In accordance with the conditions of the initial orbital energy E_{orbital} and the initial angular momentum L_{initial}, the motion of the binary systems can be classified as bound (circular or elliptical) and unbound (parabolic or hyperbolic) orbits (Capozziello et al. 2008; Capozziello & De Laurentis 2008; Berry & Gair 2010; De Laurentis & Capozziello 2010).

Gravitationally unbound interactions, or encounters, occur when $E_{\mathrm{orbital}} \geq 0$ without direct capture, and the trajectory of one component of the system will be either parabolic or hyperbolic relative to the other. The GW signals produced from such encounters do not resemble those from bound systems, but will instead produce a strong burst of radiation as the objects have their closest encounter. The process may be considered a gravitational analogy to Bremsstrahlung (Peters 1970).

In this work, we will focus on parabolic encounters (Bae et al. 2017) with $E_{\mathrm{orbital}} = 0$. BH encounters that correspond to parabolic orbits at infinity merge quickly if their initial angular momentum is not suitably large enough (O'Leary et al. 2009). We use the term 'parabolic BH capture' to refer to the systems that form and merge

★ E-mail: gwcf@mail.bnu.edu.cn (WG); daniel.williams@glasgow.ac.uk (DW)

in this way. In other cases, the binaries tentatively pass by and finally merge in the very distant future.

We expect the GW signal from BH capture to be detectable both in the current generation of detectors, and planned future detectors (De Vittori, Jetzer & Klein 2012; García-Bellido & Nesseris 2018). The expected event rate for hyperbolic BH encounters in galactic nuclei is comparable to estimates for other sources of GW signals, which is $\sim 0.9\,\mathrm{Gpc^{-3}\,yr^{-1}}$ (Mukherjee, Mitra & Chatterjee 2021), independent of any detector.

GW signals from BBH events have a characteristic morphology: during the inspiral, before the two BHs merge the signal is sinusoidal, with a growing frequency as the radius of the binary decreases. The remainder of the signal is produced from the merger, and the ringdown. As the total mass of the binary increases, the frequency at which the merger occurs decreases, and consequently, for high-mass systems, the merger may occur close to the lowest frequency the detector is capable of successfully observing. In such a scenario, the signal might appear to have little or no inspiral due to the lower frequency limit of ground-based detectors. The waveforms of BH encounters, or parabolic BH captures will often have no inspiral, or only a small number of cycles of inspiral. As a result, it is not implausible that an event may be misinterpretted as a high-mass BH coalescence when in fact it had been a BH capture. An example of an observation that fits these conditions is GW190521, which has been interpreted as a BBH coalescence with a total mass around $142\,\mathrm{M_\odot}$ (Abbott et al. 2020a,b; Nitz et al. 2021; Nitz & Capano 2021; Estellés et al. 2022).

The use of unmodelled 'burst' searches has been proposed for these highly eccentric mergers (Tiwari et al. 2016; Abbott et al. 2019b; Ramos-Buades et al. 2020), though they are less capable of digging deep into the noise for signals and their sensitivity is hard to quantify (Klimenko et al. 2016). Therefore, it is probable that GW190521-like signals will be detected using analyses designed to identify and analyse BBH signals in the future, rather than those designed for more exotic waveform morphologies. At present, parameter estimation analyses using an approximant for parabolic capture signals is not viable due to a lack of sufficiently flexible waveform models. We therefore ask if analyses using BBH waveform models will produce different, and distinguishable, results when used to analyse both BBH and parabolic capture signals. In order to do this, we conducted two sets of analyses: one analysing simulated BBH signals injected into simulated noise and one analysing simulated parabolic capture signals in simulated noise. We then compare the posterior probability distributions of the BBH and parabolic capture injections.

The conventional approach for parameter estimation used in GW analysis uses Bayesian inference and stochastic sampling, which usually requires a large amount of computation. Therefore, a neural network that can quickly give a posterior under BBH model while maintaining a fairly high accuracy was employed. Comparative studies of such a neural network approach and conventional Bayesian parameter estimation techniques have shown that a properly trained neural network is capable of emulating a posterior distribution to an acceptable level of accuracy (Gabbard et al. 2021). Given the large amount of simulated data required for our study, we used the network to obtain the posteriors for each simulation. We compare the mass, distance, and merger time posterior distributions using the Jensen–Shannon (JS) divergence (Lin 1991) to quantify any differences between these posteriors for the simulated population of BH captures and BBH signals.

The outline of this paper is as follows. In Section 2, we describe the production of the simulated parabolic BH capture and BBH signals thate used for the analysis. In Section 3, we describe the parameter estimation method, and the use of a deep learning approach to improve computing speed. The results of this analysis are presented in Section 4. Finally, the main outcomes of the work and possible future directions are summarized in Section 5.

2 MOCK DATA CREATION

Recent advances in numerical relativity (Bae et al. 2017) have allowed the production of gravitational waveforms for unequal mass BH encounters under the parabolic approximation, which were used in this work. The generated waveforms are applicable for non-spinning pairs of BHs with relative velocity up to $10 \sim 20$ per cent of the speed of light. The four waveforms we used to produce our mock data are from parabolic BH captures with mass ratios $q \in \{1, 4, 8, 16\}$. While these waveforms contain a merger and a ringdown, they lack the characteristic sinusoidal morphology of the inspiral.

We used the MINKE (Williams 2018) python package to generate the parabolic capture injections. MINKE is a toolkit designed to produce injection sets for signals derived from numerical relativity simulations and performs the appropriate rescaling required to produce waveforms for systems with any total mass and at any luminosity distance. The signal is then convolved with the detector's antenna pattern and time shifted for the corresponding detector. The process for producing the mock data set using MINKE is as follows.

For each of the four mass ratios we considered, we chose a luminosity distance and a sky location for the parabolic capture waveforms, which produced *a posterior* probability distribution when analysed by VITAMIN, which was visually similar to the posterior from analysing a high-mass BBH signal. The posterior of a typical BBH has a shape with the following features: it should have obvious peaks and narrow width of the marginal distributions, which indicates that the corresponding parameters have been inferred well under the BBH model. The maxima of the marginal distributions from BH captures are not required to be in the same locations as a typical BBH. The visual method essentially checks that the posterior distributions neither rail against nor are compressed towards one of the edges of the prior for a particular parameter. This led us choosing the waveform parameters shown in Table 1. The simulated data are created with a fixed total mass of $150\,\mathrm{M_\odot}$ and a luminosity distance d_0 in [100, 8000] Mpc. Here, and elsewhere in this work, masses are quoted in the detector frame. The right ascension and declination, α, δ, and the waveform polarization, ψ were distributed uniformly for all waveforms. The detectors we used are LIGO Handford (H1), LIGO Livingston (L1; Aasi et al. 2015), and Virgo (V1; Acernese et al. 2014).

The start time t_{start} was specified when generating mock signal, while the merger time t_0 and signal length could not be. For the parabolic BH capture waveforms with a mass ratio of 1, 4, 8, and 16, the length of the raw data produced by MINKE ranges from 0.88 to 1.34 s. We manually truncated the time series, or padded it with zeros, to fit the 1-s analysis constraint of VITAMIN. At the same time, we put the signal's peak at $t_0 = 0.22$ s, which lies within the pretrained prior range [0.15, 0.35] s expected by VITAMIN. To make the network function properly, signals were processed in the same way as the training data. VITAMIN requires that the input data are whitened using detector amplitude spectral density (ASD), and given a zero mean, unit variance Gaussian noise. This whitening process was adopted mainly to scale the data more properly for input to the
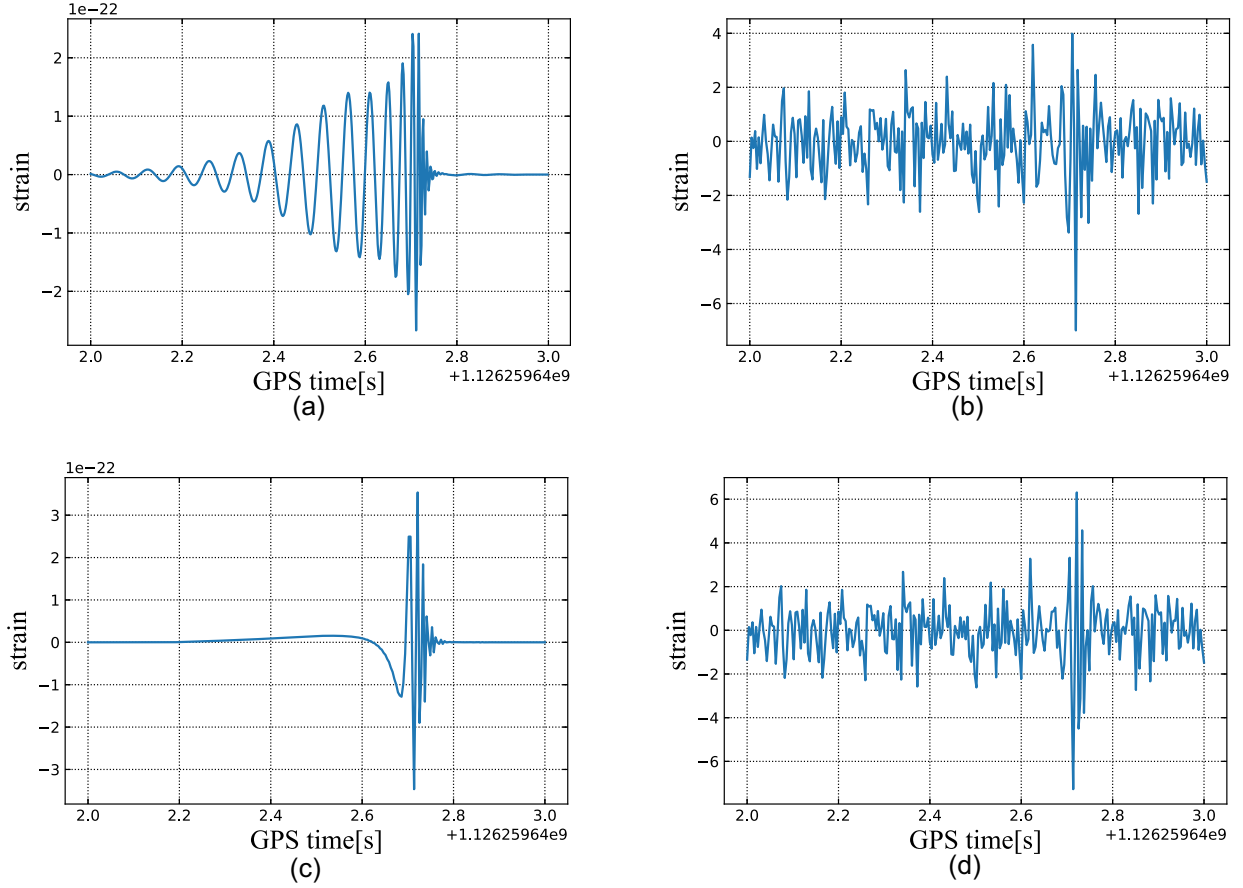
Figure 1. Examples of BBH and parabolic BH capture injections are used in this work. The panels on the left show the signal before injection, and those on the right show the signal whitened against the power spectrum of the simulated detector noise. In the top row, (a) represents a typical high-mass BBH signal for a system with $m_1 = 78\,\mathrm{M_\odot}$, $m_2 = 72\,\mathrm{M_\odot}$ at a distance of 1400 Mpc and (b) depicts the signal from (a) whitened. In the bottom row, (c) represents a parabolic BH capture signal for a system with mass ratio $q = 1$, and a total mass of $150\,\mathrm{M_\odot}$ at a distance of 5000 Mpc, with (d) depicting it whitened. All waveforms in this paper correspond to a three-detector configuration, while here we only show the signal in H1 detector.

Table 1. The injections of parabolic BH capture mock data used for VITAMIN analysis. We list the start time t_{start}, the reference time t_{ref} in GPS time, and the fixed merger time $t_0 = 0.22\,s$, where the merger time in GPS time $t_{\mathrm{merger}} = t_{\mathrm{ref}} + t_0$. Here, and elsewhere in this work, masses are quoted in the detector frame.

Parameter	Injection
m_{total} (M$_\odot$)	150
d_{L} (Mpc)	d_0
t_0 (s)	0.22
α	$(0, 2\pi)$
δ	$(-\pi/2, \pi/2)$
ψ	$(0, 2\pi)$
Duration (s)	1
t_{start} (GPS time)	1126259642
t_{ref} (GPS time)	1126259642.5
Detector network	H1, L1, V1

neural network, and we employed aLIGO zero detuning,[1] high power design sensitivity ASD for H1 and L1, and the advanced Virgo[2] ASD

for V1. Examples of BBH and parabolic BH capture injections are showed in Fig. 1.

3 ANALYSIS

The most widely used approach to analysing BBH signals uses Bayesian inference (Veitch & Vecchio 2008, 2010). One analysis pipeline that is widely used is BILBY (Ashton et al. 2019; Romero-Shaw et al. 2020a), a modular PYTHON package. However, it is computationally intensive because it uses stochastic sampling techniques to estimate the posterior. Instead, we used VITAMIN (Gabbard et al. 2021) to produce rapid posterior estimates for each injection. Due to the high-mass systems we focus on, we first used the pre-training function supported by VITAMIN to expand its prior parameter space to Table 2. Once we obtained a posterior that is visually similar to that for a BBH, we applied Bayesian inference to the corresponding signal using non-spinning and spinning BBH templates. For the two inferences, we employed the IMRPhenomPv2 (Ajith et al. 2007; Khan et al. 2016) approximant, respectively[3] because it was used

[3] IMRPhenomPv2 has six parameters to model the spins of BBH system. In order to produce non-spinning waveforms from it, we set the six spins as zero.

Table 2. The priors and fixed parameter values used on non-spinning BBH model parameters for VITAMIN analysis.

Parameter	min	max	prior
$m_{1,2}$ (M$_\odot$)	30	160	uniform
$d_{\rm L}$ (Mpc)	1000	3000	uniform
t_0 (s)	0.15	0.35	uniform
α	0	2π	uniform
δ	$-\pi/2$	$\pi/2$	cosine
θ_{jn}	0	π	sine
spins	0		-
duration (s)	1		-
$t_{\rm start}$ (GPS time)	1126259642.0		-
$t_{\rm ref}$ (GPS time)	1126259642.5		-
detector network	H1, L1, V1		

to train VITAMIN. We carried-out these analyses using BILBY as a corroboration for VITAMIN analysis.

3.1 Bayesian inference

The probability distribution on a set of parameters, conditional on the measured data, can be determined using Bayes Theorem, which can be represented as

$$p(x|y) = \frac{p(y|x)p(x)}{p(y)}, \tag{1}$$

where x are the parameters, y are the observed data, $p(x)$ is the prior on the parameters, $p(y)$ is the probability of the data, $p(x|y)$ is the posterior, and $p(y|x)$ is the likelihood.

GW parameter estimation analyses typically require the exploration of a very large parameter space while analysing a large volume of data. To address this, it is typical to use a stochastic sampler to reconstruct the posterior. This sampling can be done with a variety of techniques, including Nested Sampling and Markov chain Monte Carlo (Hastings 1970; Christensen & Meyer 2001; Cornish & Crowder 2005) methods. The popular software packages used by LIGO parameter estimation analyses are LALINFERENE and BILBY, which offer multiple sampling methods. We used BILBY, a Bayesian inference library for GW astronomy, as an interface for the DYNESTY (Speagle 2020) sampler.

Once the appropriate posteriors had been obtained in Section 3.2, one example of the corresponding signals was expanded with a data segment of 4 s and a sampling rate of 1024 Hz for a precise analysis. We used the DYNESTY sampler and both spinning and non-spinning BBH waveforms drawn from the IMRPhenomPv2 model to perform parameter estimation on the data. The priors we used are shown in Tables 3 and 4.

We then calculated the Bayes factors K for non-spinning BBH-template and spinning BBH-template against the noise. The Bayes factor is defined as

$$K = \frac{p(y|x, H_1)}{p(y|x, H_2)} = \frac{\int p(x_1|H_1)p(y|x_1, H_1){\rm d}x_1}{\int p(x_2|H_2)p(y|x_2, H_2){\rm d}x_2}, \tag{2}$$

where H_1 and H_2 are two different hypotheses. With a $K > 1$ indicating greater support for H_1 hypothesis.

Finally, we used the median recovered values from the parabolic capture signal posterior to create injections using two BBH models (one spinning and one non-spinning). These two recovered signals were compared with the corresponding parabolic capture, demonstrating the ability of a parabolic capture to mimic a high-mass BH when analysed with the IMRPhenomPv2 waveform approximant.

Table 3. The priors and fixed parameter values used on non-spinning BBH model parameters for BILBY analysis. In this analysis, we use a 4-s duration time series.

Parameter	Min	Max	Prior
$m_{1,2}$ (M$_\odot$)	30	160	uniform
$d_{\rm L}$ (Mpc)	1000	3000	uniform
t_0 (s)	0.15	0.35	uniform
α	0	2π	uniform
δ	$-\pi/2$	$\pi/2$	cosine
θ_{jn}	0	π	sine
ψ	0	π	uniform
ϕ	0	2π	uniform
spins	0		-
duration (s)	4		-
$t_{\rm start}$ (GPS time)	1126259642.0		-
$t_{\rm ref}$ (GPS time)	1126259644.5		-
detector network	H1, L1, V1		

Table 4. The priors and fixed parameter values used on spinning BBH model parameters for BILBY analysis. In this analysis, we use a 4-s duration time series.

Parameter	Min	Max	Prior
$m_{1,2}$ (M$_\odot$)	30	160	uniform
$d_{\rm L}$ (Mpc)	1000	3000	uniform
t_0 (s)	0.15	0.35	uniform
α	0	2π	uniform
δ	$-\pi/2$	$\pi/2$	cosine
θ_{jn}	0	π	sine
ψ	0	π	uniform
ϕ	0	2π	uniform
$a_{1,2}$	0	0.99	uniform
$\theta_{1,2}$	0	π	sine
$\Delta\phi$	0	2π	uniform
ϕ_{JL}	0	2π	uniform
duration (s)	4		-
$t_{\rm start}$ (GPS time)	1126259642.0		-
$t_{\rm ref}$ (GPS time)	1126259644.5		-
detector network	H1, L1, V1		

3.2 VITAMIN analysis

VITAMIN is a recently proposed network for BBH signals based on a conditional variational auto-encoder (Pagnoni, Liu & Li 2018; Tonolini et al. 2020), which has been shown to produce samples describing the posterior distribution six orders of magnitude faster than the traditional Bayesian approach (Gabbard et al. 2021). The network used non-spinning BBH approximant IMRPhenomPv2. It omits the six additional parameters required to model the spins of the BBH system and produces posteriors on eight parameters: the component masses m_1, m_2, the luminosity distance $d_{\rm L}$, the time of coalescence t_0, the binary inclination θ_{jn}, right ascension α, and declination δ. The phase at coalescence ϕ_0 and the GW polarization angle ψ are internally marginalized out. For each parameter, we used a uniform prior, with the exception of the declination and inclination parameters for which we used priors that were uniform in $\cos(\delta)$ and $\sin\theta_{jn}$. The corresponding prior ranges are defined in Table 2. The initial prior range of VITAMIN focuses on low-mass BH binaries, and the upper limit of the component mass is 80 M$_\odot$. However, we trained the network with a customized prior, increasing the maximum component mass to 160 M$_\odot$ to deal with

Table 5. The d_L injections to produce VItamin posteriors that are visually similar to BBH. It decreases with the increase in the mass ratio q.

Mass ratio q	d_L injection (Mpc)
1	5000
4	2000
8	1500
16	500

the high-mass BBH system in this study. The BBH signals used as training and test data were produced using IMRPhenomPv2, with a minimum cutoff frequency of 20 Hz. The training procedure only needed to be performed once, and took $\mathcal{O}(1)$ day to complete. The resulting trained network could then quickly generate samples describing the posterior distribution, which was proved to achieve the same accuracy of results as trusted benchmark analyses used within the LIGO-Virgo Collaboration (Gabbard et al. 2021). For BBH signals, GW data are usually sampled to frequencies between 1 and 16 kHz, depending upon the mass of binary. We have chosen a low sampling rate of 256 Hz for the VITAMIN network to decrease the computational time required to train it. We observed that the main frequency component of BH capture signals with total mass of 150 $M_{\odot}$ is around 80 Hz, which is below Nyquist sampling rate $f_{\text{Nyquist}} = 128$ Hz, thus the signal is well covered by the sampling range.

For all parabolic BH capture waveforms, we used one set of sky location injections (α, δ, and ψ) that contains 100 samples. We only adjusted d_L injection for the appropriate posteriors, which were given by the VITAMIN network rapidly once the data had been input. d_L injection is a critical factor due to the effect of waveform scaling. It must be chosen such that the injected waveform has an SNR that would be detectable and produce a plausible posterior distribution that might be mistaken as that of a high-mass BBH.

4 RESULTS

In the VITAMIN recovery study on parabolic BH capture using non-spinning BBH approximate IMRPhenomPv2, we did obtain the posteriors look superficially like a BBH posterior.[4] The d_L injections to produce such posteriors are recorded in Table 5. We calculated the optimal SNR in each detector, which is defined as

$$\rho_{\text{opt}} = 2 \left[\int_{f_{\min}}^{f_{\max}} \frac{|h^2(f)|}{S_h(f)} \, df \right]^{\frac{1}{2}}, \tag{3}$$

where $h(f)$ is the Fourier transform of the (time-domain) GW signal, $S_h(f)$ is the one-sided noise spectral density in units of Hz^{-1}, and $f_{\min} \leq f \leq f_{\max}$ correspond to the frequency band of the instrument. We found that, in the step of adjusting d_L injection, waveforms with a higher mass ratio produced a detectable SNR to smaller luminosity distances.

We also conducted parameter estimation using BILBY on one parabolic capture signal, with the posterior distribution sampled by DYNESTY.[5] Both spinning and non-spinning BBH templates

[4]The posterior probability distribution of a parabolic BH capture that mimics a BBH determined by VITAMIN could be seen in Fig. A1. As a comparison, we also display the VITAMIN posterior of a typical high-mass BBH in Fig. A2.

[5]The posterior probability distributions for a parabolic capture signal analysed by BILBY is shown in Figs A3 and A4 using non-spinning and spinning models, respectively.

IMRPhenomPv2 have a high log Bayes factor $\ln K = 134.620^{\pm 0.168}$, $117.134^{\pm 0.155}$ against noise, strongly supporting the hypothesis that the signal is a BBH merger. As a comparison, the reference BBH data gives a log Bayes factor $\ln K = 157.363^{\pm 0.209}$ compared to the noise hypothesis in the non-spinning BBH analysis. Then we have the log Bayes factor between spinning and non-spinning BBH templates $\ln K = 17.486^{\pm 0.229}$, which is quite small. This illustrates that it is very difficult for the Bayes factor to distinguish between the spinning and non-spinning models in this case. We then generated the signal corresponding to the median values of each waveform parameter's posterior, and compared it with the original signal from Fig. 2, and we show the whitened waveforms of both the parabolic BH capture signal and the recovered BBH signal overlaid. Here, we can see the strong similarity in the merger-ringdown phase.

Furthermore, we might be able to make a case that the resemblance is more than superficial by reference to a statistic. To do this, we calculate the JS divergence (Lin 1991) between the posterior distributions calculated by analysing both injected BBH signals and injected parabolic capture waveforms. If the posterior distributions from an injected BBH and an parabolic capture signal are not statistically distinctive, they will have a small JS divergence, and we can infer that the use of the incorrect waveform model in the analysis would not be detected. The JS divergence is a symmetrized and smoothed measure of the distance between two probability distributions $p(x)$ and $q(x)$ defined as

$$D_{\text{JS}}(p \mid q) = \frac{1}{2} \left[D_{\text{KL}}(p \mid s) + D_{\text{KL}}(q \mid s) \right], \tag{4}$$

where $s = 1/2(p + q)$ and D_{KL} is the Kullback–Leibler divergence between the distributions $p(x)$ and $q(x)$ expressed as

$$D_{\text{KL}}(p \mid q) = \int p(x) \log_2 \left(\frac{p(x)}{q(x)} \right) dx. \tag{5}$$

JS divergence ranges between [0, 1], a greater value of which indicates that the posteriors from two signals have a greater difference therefore they could be well distinguished. The two JS divergences we considered are:

(i) $D_{\text{JS, noise}}$: the divergence between posteriors of reference BBH signal with different white noise realizations.

(ii) $D_{\text{JS, ref}}$: the divergence between posteriors of parabolic capture and reference BBH signal, with the same noise realization.

$D_{\text{JS, noise}}$ reflects the volatility of the VITAMIN results when dealing with different white noise, whereas $D_{\text{JS, ref}}$ represents the bias of the IMRPhenomPv2 template when modelling parabolic BH capture signals. We expect that $D_{\text{JS, ref}}$ should be obviously greater than the $D_{\text{JS, noise}}$, in this case calculating $D_{\text{JS, ref}}$ could be considered as a fast approach to distinguish BBH and parabolic BH capture events.

We then created mock data for the JS divergence analysis. For each parabolic BH capture waveform, we reproduced one signal that can generate a posterior, which is visually similar to one from a BBH. We analysed 100 noise realizations with the same signal injected and produced injections at the same sky location. As a result, by considering the same injection time t_0, the antenna pattern is the same for each waveform. The injections and corresponding posterior peaks from the recovery are presented in Table 6. For reference, we also analysed 100 noise realizations with BBH signals, where the signal parameters: total mass, right ascension α, declination δ, and merger time t_0, are the same as the parabolic BH capture. d_L was changed in order to scale the BBH signal's amplitude to be similar to the parabolic BH capture by visual comparison. Its injections and
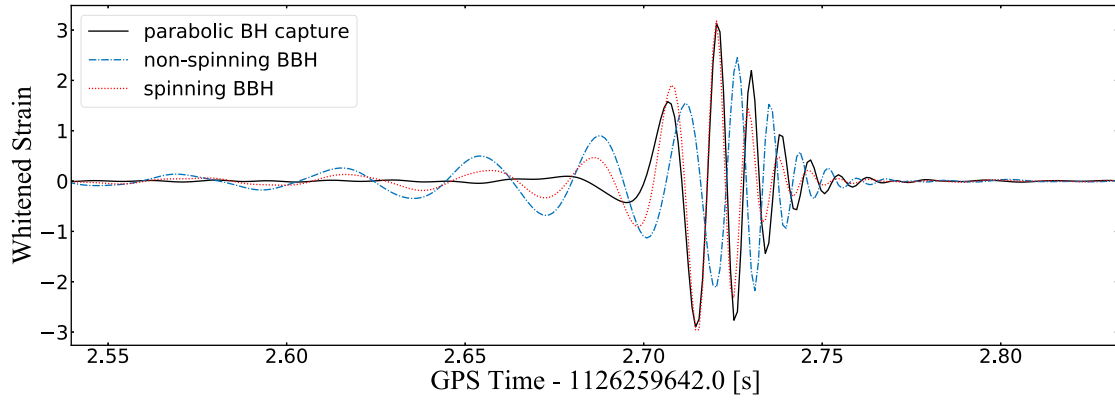
Figure 2. The whitened parabolic BH capture and the whitened recovered BBH signals at detector H1. The waveform with mass ratio $q = 1$ was injected with a total mass of 150 $M_\odot$ at a distance of 5000 Mpc. The parameter estimation was then performed on the signal using non-spinning and spinning BBH model `IMRPhenomPv2` by `BILBY`. Here, we present the waveform corresponding to the median values of each parameter's posterior distribution.

Table 6. The injections of mock signals used for JS divergence analysis, including parabolic BH capture, its recovered BBH, and reference BBH. For parabolic BH capture, we took the average peak value of `VITAMIN` posterior as the recovered injection. The inefficiency and bias introduced by analysing the parabolic BH capture signal with a non-spinning BBH model `IMRPhenomPv2` can be seen clearly, as waveforms with a higher mass ratio were recovered to a higher total mass and lower luminosity distance with a detectable SNR. NB: ψ is marginalized in `VITAMIN` inference, so we used $\psi = 0$ for the injection. θ_{jn} is not an effective parameter for the parabolic BH capture waveform. We also note that the start time $t_{\mathrm{start}} = 1126259642.0$, the reference time $t_{\mathrm{ref}} = 1126259642.5$ in GPS time, and the merger time $t_{\mathrm{merger}} = t_{\mathrm{ref}} + t_0$.

Mock signal	m_1 ($M_\odot$)	m_2 ($M_\odot$)	d_L (Mpc)	t_0 (s)	α	δ	ψ	θ_{jn}	Network SNR
Parabolic BH capture m1	75	75	5000	0.22	0.89	−0.94	1.54	-	11.13
Recovered BBH	76	68	1624	0.25	1.69	1.20	-	1.33	10.76
Parabolic BH capture m4	120	30	2000	0.22	0.89	−0.94	1.54	-	7.63
Recovered BBH	88	75	2278	0.26	4.69	1.21	-	1.76	4.38
Parabolic BH capture m8	133.3	16.7	1500	0.22	0.89	−0.94	1.54	-	9.93
Recovered BBH	98	83	1804	0.26	4.66	1.23	-	1.78	6.77
Parabolic BH capture m16	141.2	8.8	500	0.22	0.89	−0.94	1.54	-	13.90
Recovered BBH	104	90	1647	0.26	1.94	1.24	-	1.30	11.86
Reference BBH	78	72	1400	0.22	0.89	−0.94	1.54	1.51	11.27

corresponding posterior peaks from the recovery are also shown in Table 6.

In this way, we created a situation where two similar-looking GW events, one BBH and one parabolic capture, were observed. We then computed the JS divergence between their posteriors to measure their similarity. We note that while eight parameters can be inferred for a input signal by `VITAMIN`, the three parameters that showed the greatest JS divergences were the component masses, m_1, m_2 and the merger time, t_0.

Having computed the JS divergence for all 100 pairs of signals, we looked at the distribution of the divergences in Fig. 3, where the three subplots represent the JS divergences of the components masses m_1, m_2, and the merger time t_0. The distribution of $D_{\mathrm{JS,\ noise}}$ is generally close to zero, suggesting that the effect of noise on `VITAMIN`'s posterior is rather limited as we hope. We calculated D_{90}, the 90 per cent confidence interval of $p(D_{\mathrm{JS,\ noise}})$, and used this as a threshold. Then the percentage of $D_{\mathrm{JS,\ ref}}$, which is higher than this threshold, can indicate how far the distribution of $D_{\mathrm{JS,\ ref}}$ is away from the noise benchmark. The related result is recorded in Table 7. The D_{90} are 0.121, 0.134, and 0.309 for m_1, m_2, and t_0, respectively. Though D_{90} of t_0 is noticeably larger than those of the component masses of high, there is a large gap between distributions of $D_{\mathrm{JS,\ noise}}$ and $D_{\mathrm{JS,\ ref}}$ for this parameter, the percentage of which reaches 100 per cent for three waveforms and 97 per cent for the other one. The

greatest difference between the posteriors comes from the bias of the BBH approximatant `IMRPhenomPv2`. For the same injection $t_0 = 0.22$ s, a BBH signal is recovered with a peak value of 0.22 s, but a parabolic BH capture is more likely to be recovered slightly later with a recovered peak value of 0.25 or 0.26 s (See this in Table 6). Therefore, this bias can be demonstrated through the the JS divergence analysis and used to test if a signal is a parabolic BH capture. Besides, we also find that, for m_1, the average percentage of $D_{\mathrm{JS,\ ref}}$ above D_{90} is 79.5 per cent, which has a more discriminative effect than that of m_2. Parabolic captures with a mass ratio of 8 and 16 can be distinguished fairly well from BBH signals, and the lowest percentage of them that is higher than the threshold is also as high as 85 per cent. This means we could have great confidence to distinguish the two types of signals when analysing with a BBH waveform.

However, under a more realistic detection scenario, we have no access to the true parameters of the signal. Thus, in addition to calculating $D_{\mathrm{JS,\ ref}}$, we should also compare the posteriors of the parabolic BH capture and its recovered signal and look for the evidence of the bias. Therefore, the recovered peak values were taken the average from 100 samples and used to inject the non-spinning BBH model `IMRPhenomPv2` with the same noise realization. The injections are recorded in Table 6. The new JS divergence we introduce is:
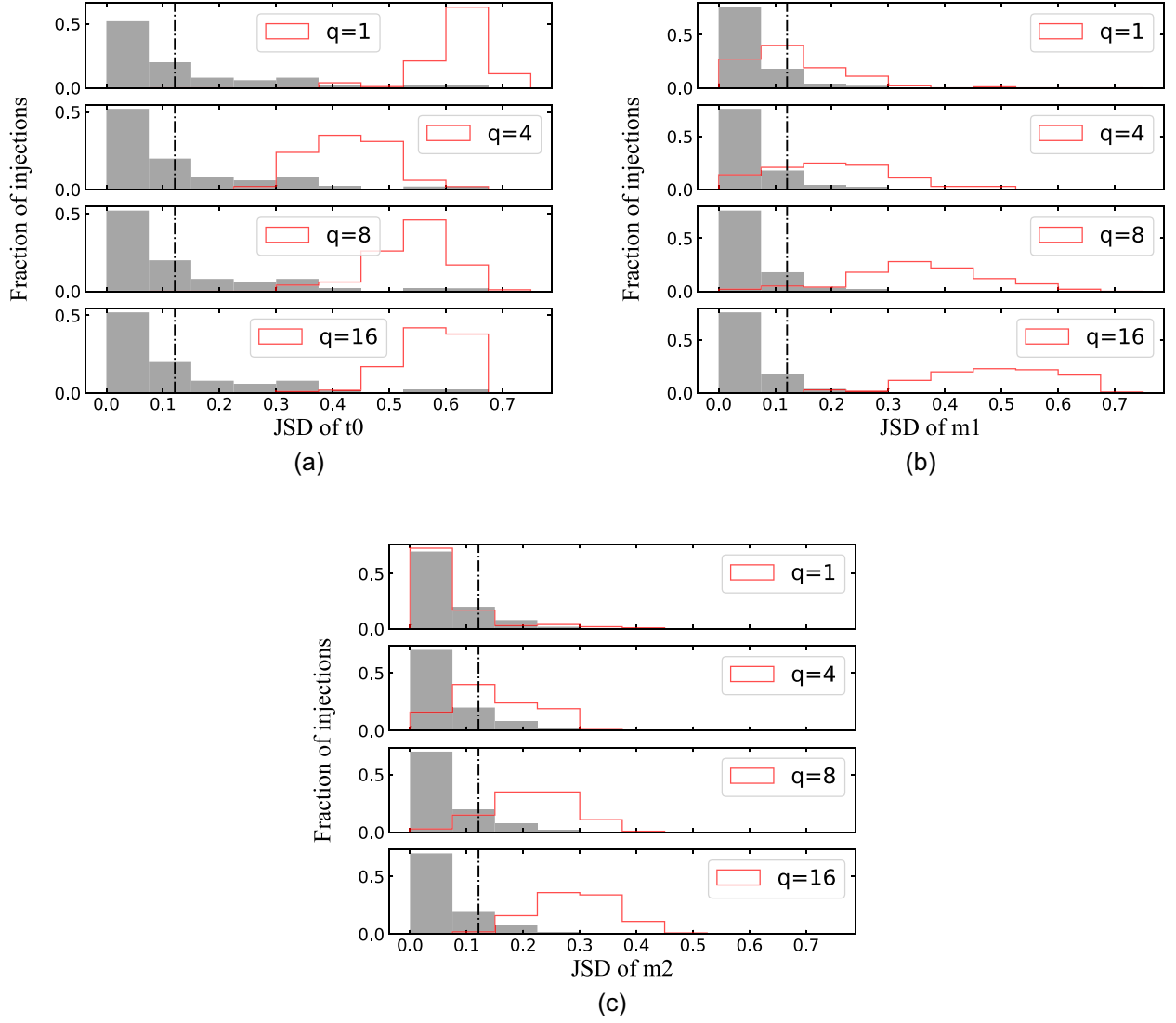
Figure 3. Distributions of the JS divergence between parabolic BH capture and reference BBH $D_{JS, ref}$ shown as the outline histograms and the JS divergence between reference BBHs with different noise $D_{JS, noise}$, shown as the shaded histogram. The JS divergence analysis is performed for four waveforms with mass ratio $q = 1$, 4, 8, and 16 and three parameters m_1, m_2, and t_0, respectively. We evaluated our distinguishing method in terms of stability and effectiveness. The former is illustrated by very low distributions of $D_{JS, noise}$, which have 90 per cent upper limit, shown as a dashed line, of m_1, m_2, and t_0 at 0.121, 0.134, and 0.309. The latter is demonstrated by a high gap between distributions of $D_{JS, noise}$ and $D_{JS, ref}$, especially regarding JS divergence of t_0. The exact information about it is presented in Table 7. This demonstrates that our approach works well.

Table 7. The percentage of $D_{JS, ref}$ and $D_{JS, recover}$ is higher than the noise threshold for parabolic BH capture waveform with a mass ratio of 1, 4, 8, and 16. The threshold is represented by $D_{JS, noise}$ at 90 per cent confidence level, which is 0.309, 0.121, and 0.134 for t_0, m_1, and m_2, respectively.

	Mass ratio	t_0	m_1	m_2
$D_{JS, ref}$	1	100 %	49 %	11 %
	4	97 %	74 %	52 %
	8	100 %	95 %	86 %
	16	100 %	100 %	100 %
$D_{JS, recover}$	1	9 %	28 %	24 %
	4	46 %	62 %	64 %
	8	19 %	32 %	27 %
	16	8 %	32 %	27 %

(i) $D_{JS, recover}$: the JS divergence between the posterior of a parabolic BH capture and its recovered BBH signal injected using the recovered peak values, with the same noise realization.

$D_{JS, recover}$ describes the effect of recovering parabolic BH capture. If the input signal is actually a BBH merger, its recovered signal should have a very similar posterior probability density distribution. In this case, the distribution of $D_{JS, recover}$ is close to zero but slightly higher due to the noise, of which the effect can be represented by $D_{JS, noise}$. But for other signals, if the difference between the posteriors of the recovered signal and itself is great, then $D_{JS, recover}$ could be used as a criterion.

We plotted the distributions of $D_{JS, recover}$ and compared it with the noise benchmark in Fig. 4. Three subplots represent JS divergence of m_1, m_2, and t_0. However, it almost overlaps with the distributions of $D_{JS, noise}$ for the three parameters, which suggests a high similarity between posteriors of parabolic BH capture and the recovered high-
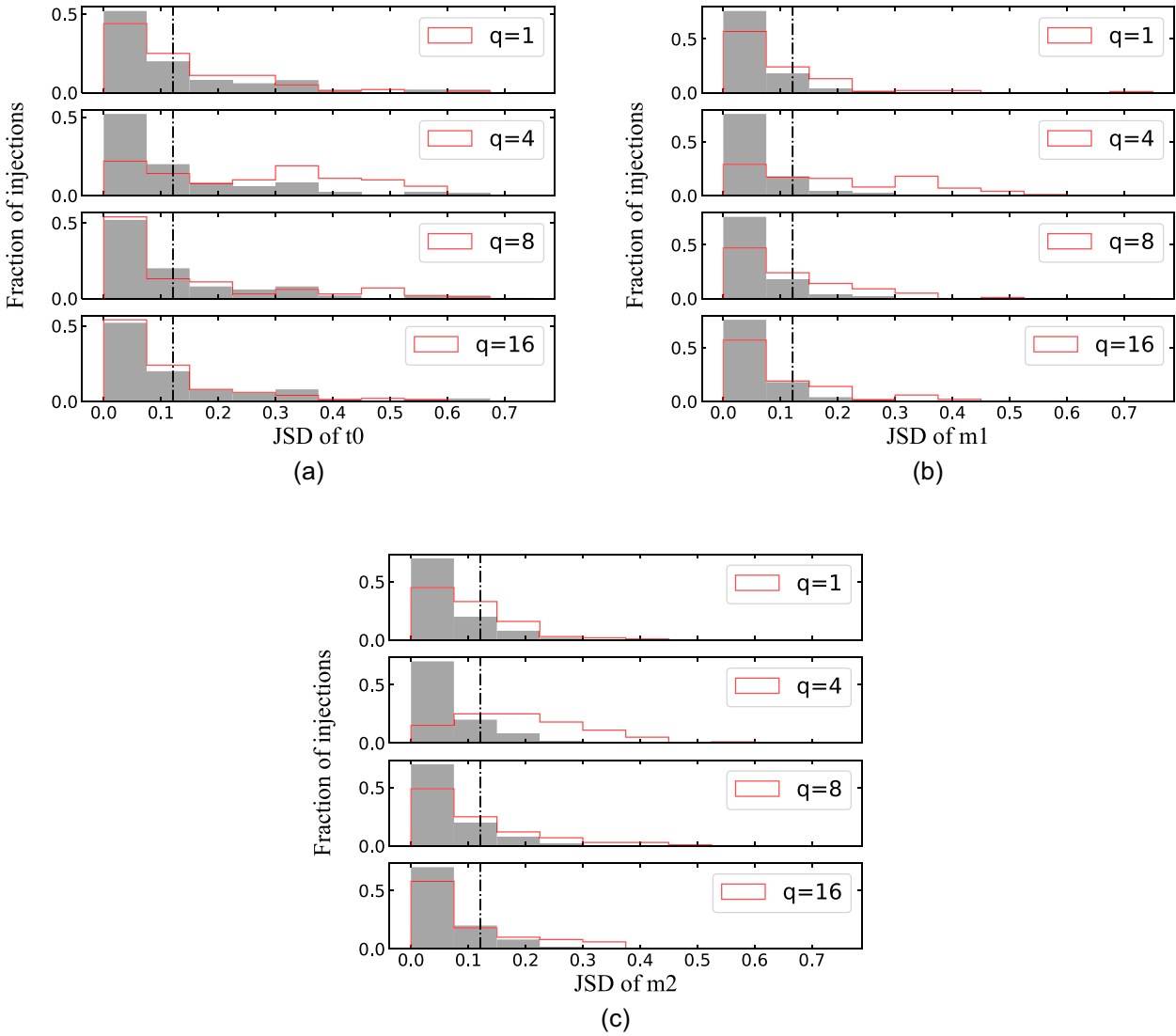
(a)

(b)

(c)

Figure 4. Distributions of the JS divergence between parabolic BH capture and its recovered BBH $D_{\mathrm{JS,\,recover}}$ shown as the outline histograms, and the JS divergence between reference BBHs with different noise $D_{\mathrm{JS,\,noise}}$ shown as a shaded histogram. The JS divergence analysis is performed for four waveforms with mass ratio $q = 1$, 4, 8, and 16 and three parameters m_1, m_2, and t_0, respectively. Here, we considered the application of our distinguishing method in more realistic scenarios and evaluated it in terms of stability and effectiveness. The stability is the same as before with very low distributions of $D_{\mathrm{JS,\,noise}}$, with the 90 per cent upper limit represented by a dashed line. However, the distributions of $D_{\mathrm{JS,\,noise}}$ and $D_{\mathrm{JS,\,recover}}$ almost overlap, which suggests that the two types of signal cannot be well distinguished in this situation. (More information about this is presented in Table 7.).

mass BBH. We also determined the percentage of $D_{\mathrm{JS,\,recover}}$ that were higher than D_{90} and recorded them in Table 7. $D_{\mathrm{JS,\,recover}}$ has a much lower percentage than $D_{\mathrm{JS,\,ref}}$ above D_{90}. Except for the waveform with mass ratio of 4, the highest percentage of their $D_{\mathrm{JS,\,recover}}$ greater than the threshold is only 32 per cent. The waveform with mass ratio of 4 is unusual compared to others, with the average percentage reaching 57.3 per cent. Since we do not know *a priori* what the mass ratio of the waveform is in the real analysis, we must consider all the waveforms equally, so this value would not be enough to provide support that the evidence of the bias has been found. In addition, $D_{\mathrm{JS,\,ref}}$ has a good performance on t_0, while $D_{\mathrm{JS,\,recover}}$ is difficult to tell apart from $D_{\mathrm{JS,\,noise}}$ as it has an average percentage of 20.5 per cent above D_{90}.

Apart from being used for JS divergence analysis, Table 6 also gives us an inspiration about the patterns on injected and recovered

parameters. First, for parabolic BH capture waveforms with mass ratios of 1, 4, 8, and 16, the total mass is recovered as 144, 163, 181, and 194 $\mathrm{M_\odot}$, respectively. These amount to a tendency for the rising of the recovered total mass with the mass ratio q increasing, and the former one is much higher than the injection of 150 $\mathrm{M_\odot}$ when the mass ratio is greater than 1. We also find that the recovered mass ratios are 1.12, 1.17, 1.18, and 1.16, respectively, which are all close to one. For comparison, GW190521 has a mass ratio of 1.29, and it is basically consistent with the analysis result we got. The sensitive distance decreases with the increase in the mass ratio q. For equal-mass BH binaries, eccentric sources are thought to be much closer than BBH sources with a circular orbit in inspiral. Another discrepancy that could be highlighted is that the recovered merger times t_0 are all about 0.04 s behind the injection truth. We suspect that it is caused by a mathematical fit of the BBH model to the capture signal, but we will investigate for a deeper pattern in the future.

5 SUMMARY AND DISCUSSION

In this work, we proposed the possibility that current approaches to GW analysis could misclassify parabolic BH capture signal as a BBH signal. We then demonstrated a scenario under which this could occur and devised for a statistical method to distinguish them. We injected parabolic BH capture waveforms to produce mock data, using a tool developed for characterizing burst searches, MINKE, which was exploited to make injection with the customized distribution. The main difficulty is that it is impossible to predict how a signal can be inferred under a biased multiparameter model, and the computational cost of traditional Bayesian inference is expensive. To overcome this, we adopted VITAMIN, a neural network based on the BBH model, and retrained it to fit high-mass BBH signals, which reduced the cost of each parameter estimation to a very low level. This greatly helped us to continuously adjust the injection parameters of the parabolic BH capture and finally obtain the appropriate posterior probability. After that, we also performed confirmatory parameter estimation using DYNESTY sampler, of which the result also had a strong statistical support.

Here, we summarize our main conclusions in more detail.

We have established that there are scenarios in which a parabolic BH capture could be recovered as a spinning (non-spinning) BBH signal with high statistical support, a log Bayes factor of $\ln K = 134.6\,(111.7)$, compared to a noise hypothesis. This type of signal is likely to be mistaken as a high-mass BBH by LIGO and Virgo. Therefore, it would be valuable to be vigilant to this possibility when a high-mass BBH system is identified in an analysis, otherwise future GW events may be misclassified. This should be considered in cases where the waveform seems to lack a clear inspiral phase.

In this study, we have built a rapid approach to describe the difference between the posteriors of BBH and parabolic BH capture signals and distinguish them. This approach is based on neural network, VITAMIN, and compares the distribution of JS divergences of three parameters m_1, m_2, and t_0 from two types of GW signals, with that of noise benchmark D_{90}. Its validity has been proved by the JS divergence between the parabolic BH capture and the reference BBH, $D_{JS,\,ref}$, which has 79.5 per cent, 62.3 per cent, and 99.3 per cent of samples over D_{90} for m_1, m_2, and t_0. However, in a more realistic detection scenario, our analysis does not yield evidence that two types of GW events are distinguishable with the current BBH Bayesian inference. This is a result of the lower value of the JS divergence between the parabolic BH capture and its recovered BBH $D_{JS,\,recover}$, containing only 38.5 per cent, 35.5 per cent, and 20.5 per cent of samples located above D_{90} for m_1, m_2, and t_0. The result of our analysis would not therefore allow us to make an identification of a GW190521-like signal. As a result, the parabolic BH capture could not be distinguished from a BBH by the current quasi-circular BBH analysis, which highlights the importance of a good BH capture approximant in the future.

We have identified the patterns on injected and recovered parameters. For four waveforms, there is a tendency for the recovered total mass to rise as the mass ratio increases; only one from the equal-mass system has a recovered total mass close to the injection of 150 M, and the total masses of the others are recovered with much higher values. The recovered mass ratios are all close to one, which we also see on GW190521 with a mass ratio of 1.29. In contrast to the pattern observed with the total mass, the sensitive distance decreases as the mass ratio increases. We also note that that the recovered merger times are all offset by around 0.04 s compared to the injected value.

The research in this paper constitutes a comparatively novel use of deep learning in GW data analysis. A typical Bayesian approach to analyses used in this study takes 8–14 h while the neural network requires around 50 s. For each waveform, there were about four iterations on average before determining the appropriate d_L injection, and each turn gave 100 Bayesian posteriors corresponding to the combinations of sky location. A total of 1600 inferences were performed in this stage. Once the posteriors that mimic BBH were obtained, we selected one signal from each waveform and analysed it with 100 noise realizations, as well as the reference BBH signal, for the construction of JS divergence distribution, of which the stage contained 500 inferences. BBH signals injected from the recovered peaks of the BH capture signals were then inferred with the same noise realization sets. This last step required 400 inferences and constructed the distribution of $D_{JS,\,recover}$ to finally describe the difference between BBH and BH capture signals. Overall, the use of a neural network saved around 2.7×10^4 h when performing 2500 parameter estimation analyses.

Because of computational cost limitations in training, the VITAMIN network has not been trained to take into account the spins of the BBH model. One promising signature of the BH binary formation environment is the angular distribution of BH spins (Farr et al. 2017). Binaries formed through dynamical interactions are expected to have isotropic spin orientations (Sigurdsson & Hernquist 1993; Portegies Zwart & McMillan 2000; Rodriguez et al. 2015; Rodriguez et al. 2016; Stone, Metzger & Haiman 2017) whereas systems formed from pairs of stars born together are more likely to have spins preferentially aligned with the binary orbital angular momentum (Belczynski et al. 2016; Mandel & de Mink 2016; Marchant et al. 2016; Stevenson et al. 2017). When modelling the BH capture data, the six additional parameters of spins, as intrinsic properties of a binary, are expected to play an important role in distinguishing binary formation channels, allowing a further precise search that has been done in the real data analysis. We will return to this subject in future work.

The component mass prior range of VITAMIN can be expanded and the sampling rate can be raised to cover more BH capture samples. These events are principally from low-frequency sources, making them ideal candidates for both Einstein Telescope (Sathyaprakash et al. 2012, 2013), which aims to achieve much greater low-frequency sensitivity than current detectors, but also for Deci-Hz detectors, such as DECIGO (Kawamura et al. 2006, 2021). The misclassification is expected to be eliminated with their ability to observe at much lower frequencies, removing the ambiguity between unobserved low-frequency inspiral cycles and a total lack of inspiral. The detection rate of BH captures is dependent on the initial mass function of stars in galactic nuclei and the mass of the most massive BHs. Therefore future observations can constrain both the average star formation properties and upper mass of BHs in galactic nuclei (O'Leary et al. 2009).

ACKNOWLEDGEMENTS

DATA AVAILABILITY

The data and code underlying this article are available in Zenodo at https://doi.org/10.5281/zenodo.6384509.

REFERENCES

Aasi J. et al., 2015, Class. Quantum Gravity, 32, 074001
Abadie J. et al., 2010, Class. Quantum Gravity, 27, 173001
Abbott B. P. et al., 2019a, Phys. Rev. X, 9, 031040
Abbott B. P. et al., 2019b, ApJ, 883, 149
Abbott R. et al., 2020a, Phys. Rev. Lett., 125, 101102
Abbott R. et al., 2020b, ApJ, 900, L13
Abbott R. et al., 2021, Phys. Rev. X, 11, 021053
Acernese F. et al., 2014, Class. Quantum Gravity, 32, 024001
Ajith P. et al., 2007, Class. Quantum Gravity, 24, S689
Ashton G. et al., 2019, ApJS, 241, 27
Bae Y.-B., Lee H. M., Kang G., Hansen J., 2017, Phys. Rev. D, 96, 084009
Belczynski K., Holz D. E., Bulik T., O'Shaughnessy R., 2016, Nature, 534, 512
Berry C. P. L., Gair J. R., 2010, Phys. Rev. D, 82, 107501
Cao Z., Han W.-B., 2017, Phys. Rev. D, 96, 044028
Capozziello S., De Laurentis M., 2008, Astropart. Phys., 30, 105
Capozziello S., de Laurentis M., de Paolis F., Ingrosso G., Nucita A., 2008, Mod. Phys. Lett., 23, 99
Christensen N., Meyer R., 2001, Phys. Rev. D, 64, 022001
Collaboration T. L. S. et al., 2021, GWTC-3: Compact Binary Coalescences Observed by LIGO and Virgo During the Second Part of the Third Observing Run. preprint (arXiv:2111.03606)
Cornish N. J., Crowder J., 2005, Phys. Rev. D, 72, 043005
De Laurentis M., Capozziello S., 2010, Mem. Soc. Astron. Ital., 81, 87
De Vittori L., Jetzer P., Klein A., 2012, Phys. Rev. D, 86, 044017
Estellés H. et al., 2022, ApJ, 924, 79
Farr W. M., Stevenson S., Miller M. C., Mandel I., Farr B., Vecchio A., 2017, Nature, 548, 426
Gabbard H., Messenger C., Heng I. S., Tonolini F., Murray-Smith R., 2021, Nature Phys., 18, 112
Gamba R., Breschi M., Carullo G., Rettegno P., Albanesi S., Bernuzzi S., Nagar A., 2021, preprint (arXiv:2106.05575)
García-Bellido J., Nesseris S., 2018, Phys. Dark Universe, 21, 61
Gayathri V. et al., 2022, Nature Astron., 6, 344
Gondán L., Kocsis B., Raffai P., Frei Z., 2018, ApJ, 860, 5
Hastings W. K., 1970, Biometrika, 57, 97
Hinder I., Vaishnav B., Herrmann F., Shoemaker D. M., Laguna P., 2008, Phys. Rev. D, 77, 081502
Kawamura S. et al., 2006, Class. Quantum Gravity, 23, S125
Kawamura S. et al., 2021, Prog. Theor. Exp. Phys., 2021, 05A105
Khan S., Husa S., Hannam M., Ohme F., Pürrer M., Forteza X. J., Bohé A., 2016, Phys. Rev. D, 93, 044007
Klimenko S. et al., 2016, Phys. Rev. D, 93, 042004
Lightman A. P., Shapiro S. L., 1978, Rev. Mod. Phys., 50, 437

Lin J., 1991, IEEE Trans. Inf. Theory, 37, 145
Liu X., Cao Z., Shao L., 2020, Phys. Rev. D, 101, 044049
Mandel I., de Mink S. E., 2016, MNRAS, 458, 2634
Marchant P., Langer N., Podsiadlowski P., Tauris T. M., Moriya T. J., 2016, A&A, 588, A50
Morscher M., Pattabiraman B., Rodriguez C., Rasio F. A., Umbreit S., 2015, ApJ, 800, 9
Mukherjee S., Mitra S., Chatterjee S., 2021, MNRAS, 508, 5064
Nagar A., Rettegno P., Gamba R., Bernuzzi S., 2021, Phys. Rev. D, 103, 064013
Nitz A. H., Capano C. D., 2021, ApJ, 907, L9
Nitz A. H., Capano C. D., Kumar S., Wang Y.-F., Kastha S., Schäfer M., Dhurkunde R., Cabero M., 2021, ApJ, 922, 76
O'Leary R. M., Kocsis B., Loeb A., 2009, MNRAS, 395, 2127
Pagnoni A., Liu K., Li S., 2018, Conditional Variational Autoencoder for Neural Machine Translation. preprint (arXiv:1812.04405)
Peters P. C., 1964, Phys. Rev., 136, B1224
Peters P. C., 1970, Phys. Rev. D, 1, 1559
Portegies Zwart S. F., McMillan S. L. W., 2000, ApJ, 528, L17
Ramos-Buades A., Tiwari S., Haney M., Husa S., 2020, Phys. Rev. D, 102, 043005
Rodriguez C. L., Morscher M., Pattabiraman B., Chatterjee S., Haster C.-J., Rasio F. A., 2015, Phys. Rev. Lett., 115, 051101
Rodriguez C. L., Zevin M., Pankow C., Kalogera V., Rasio F. A., 2016, ApJ, 832, L2
Romero-Shaw I. M., Lasky P. D., Thrane E., 2019, MNRAS, 490, 5210
Romero-Shaw I. M. et al., 2020a, MNRAS, 499, 3295
Romero-Shaw I., Lasky P. D., Thrane E., Bustillo J. C., 2020b, ApJ, 903, L5
Samsing J., MacLeod M., Ramirez-Ruiz E., 2014, ApJ, 784, 71
Sathyaprakash B. S., Schutz B. F., 2009, Living Rev. Relativ., 12, 1
Sathyaprakash B. et al., 2012, Class. Quantum Gravity, 29, 124013
Sathyaprakash B. et al., 2013, Class. Quantum Gravity, 30, 079501
Sigurdsson S., Hernquist L., 1993, Nature, 364, 423
Speagle J. S., 2020, MNRAS, 493, 3132
Stevenson S., Vigna-Gómez A., Mandel I., Barrett J. W., Neijssel C. J., Perkins D., de Mink S. E., 2017, Nature Commun., 8, 14906
Stone N. C., Metzger B. D., Haiman Z., 2017, MNRAS, 464, 946
Tiwari V. et al., 2016, Phys. Rev. D, 93, 043007
Tonolini F., Radford J., Turpin A., Faccio D., Murray-Smith R., 2020, J. Mach. Learn. Res., 21, 1
Veitch J., Vecchio A., 2008, Phys. Rev. D, 78, 022001
Veitch J., Vecchio A., 2010, Phys. Rev. D, 81, 062003
Williams D., 2018, https://ui.adsabs.harvard.edu/abs/2018zndo...1699336W
Wu S., Cao Z., Zhu Z.-H., 2020, MNRAS, 495, 466
Yang Y., Bartos I., Haiman Z., Kocsis B., Márka Z., Stone N. C., Márka S., 2019, ApJ, 876, 122
Zwart S. F. P., McMillan S. L. W., 2000, ApJ, 528, L17

APPENDIX A: FULL VITAMIN AND BILBY POSTERIORS

In this appendix, we present corner plots for the posterior distributions produced by analysing a parabolic BH capture with both VITAMIN (Fig. A1) and BILBY with a non-spinning BBH model (Fig. A3), a BBH merger injection with VITAMIN (Fig. A2), and BILBY with a spinning BBH model (Fig. A4).
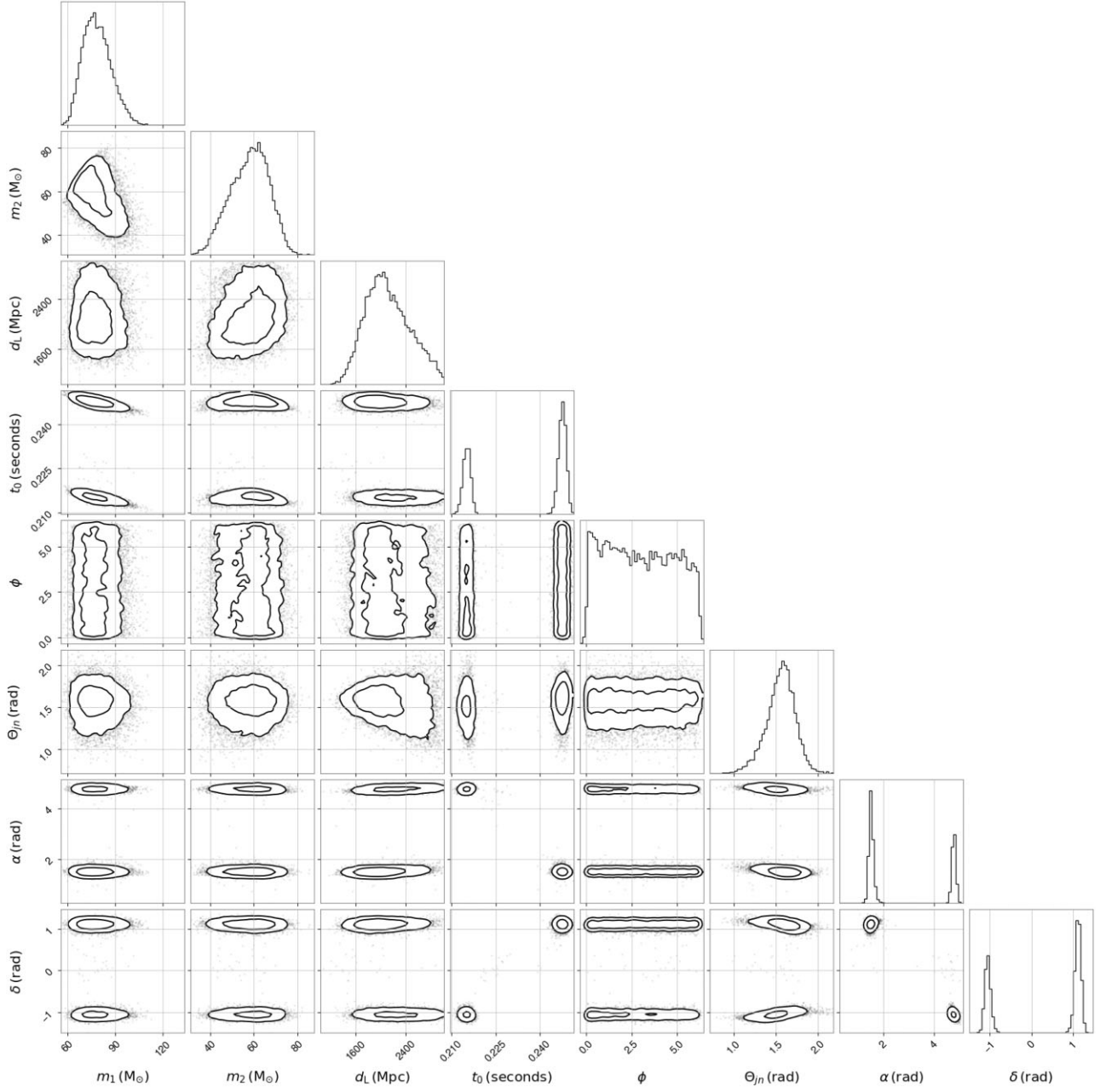
Figure A1. The posterior probability density distribution for a BH capture, recovered using a non-spinning BBH model and VITAMIN.
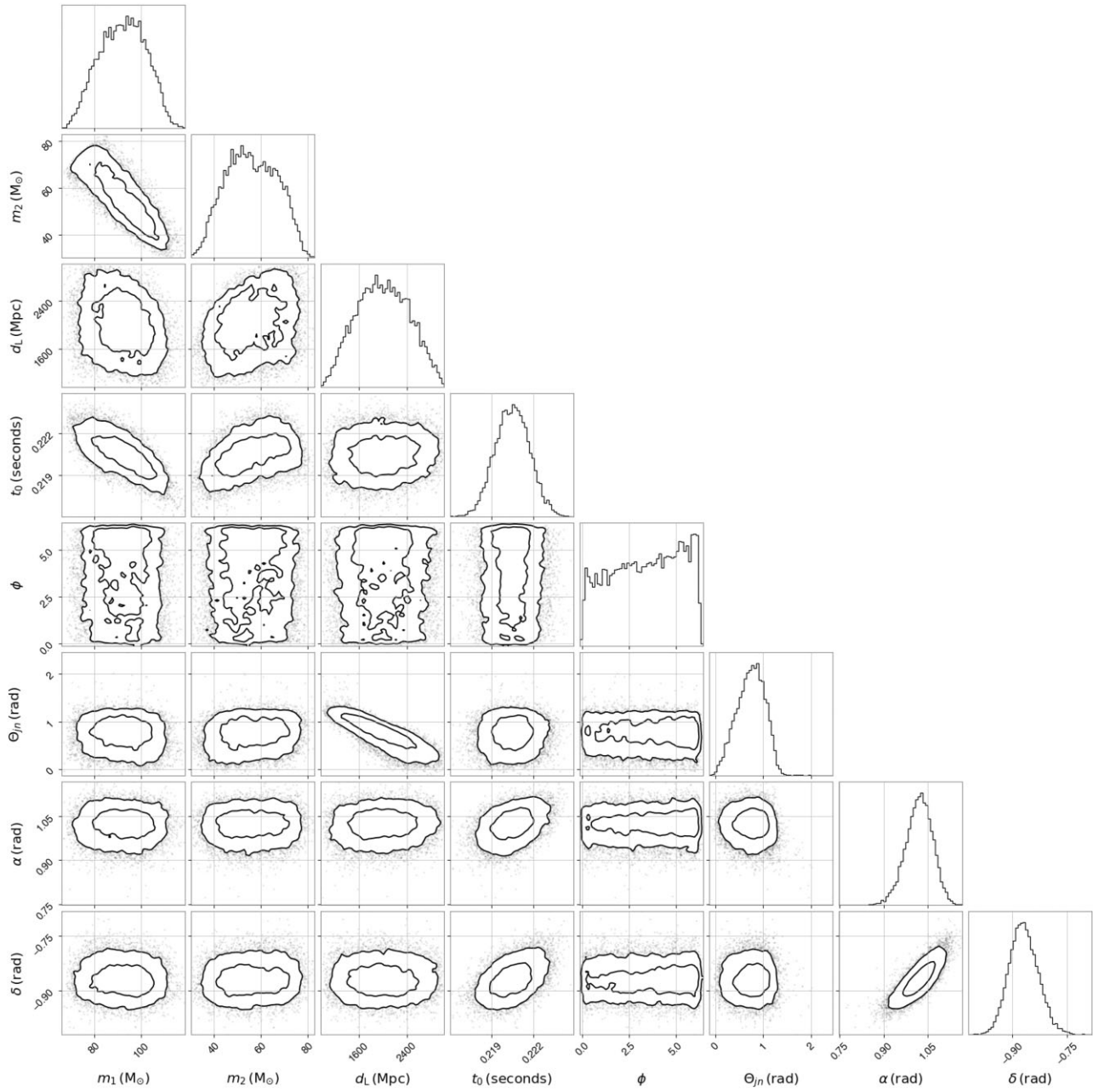
Figure A2. The posterior probability density distribution for a BBH, recovered using a non-spinning BBH model and VITAMIN.
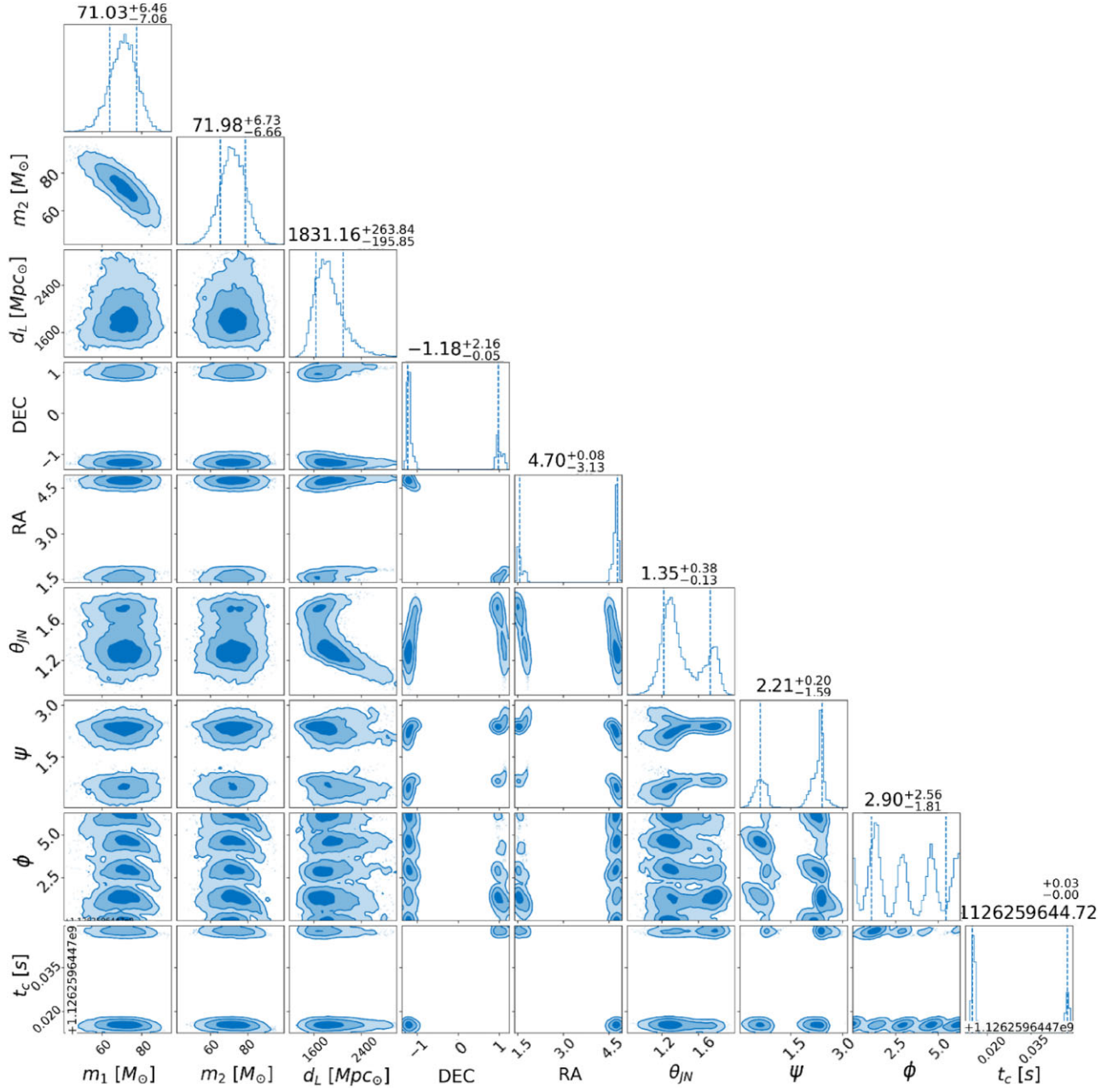
Figure A3. The posterior probability density distribution for a BH capture, recovered using a non-spinning BBH model and the DYNESTY sampler.
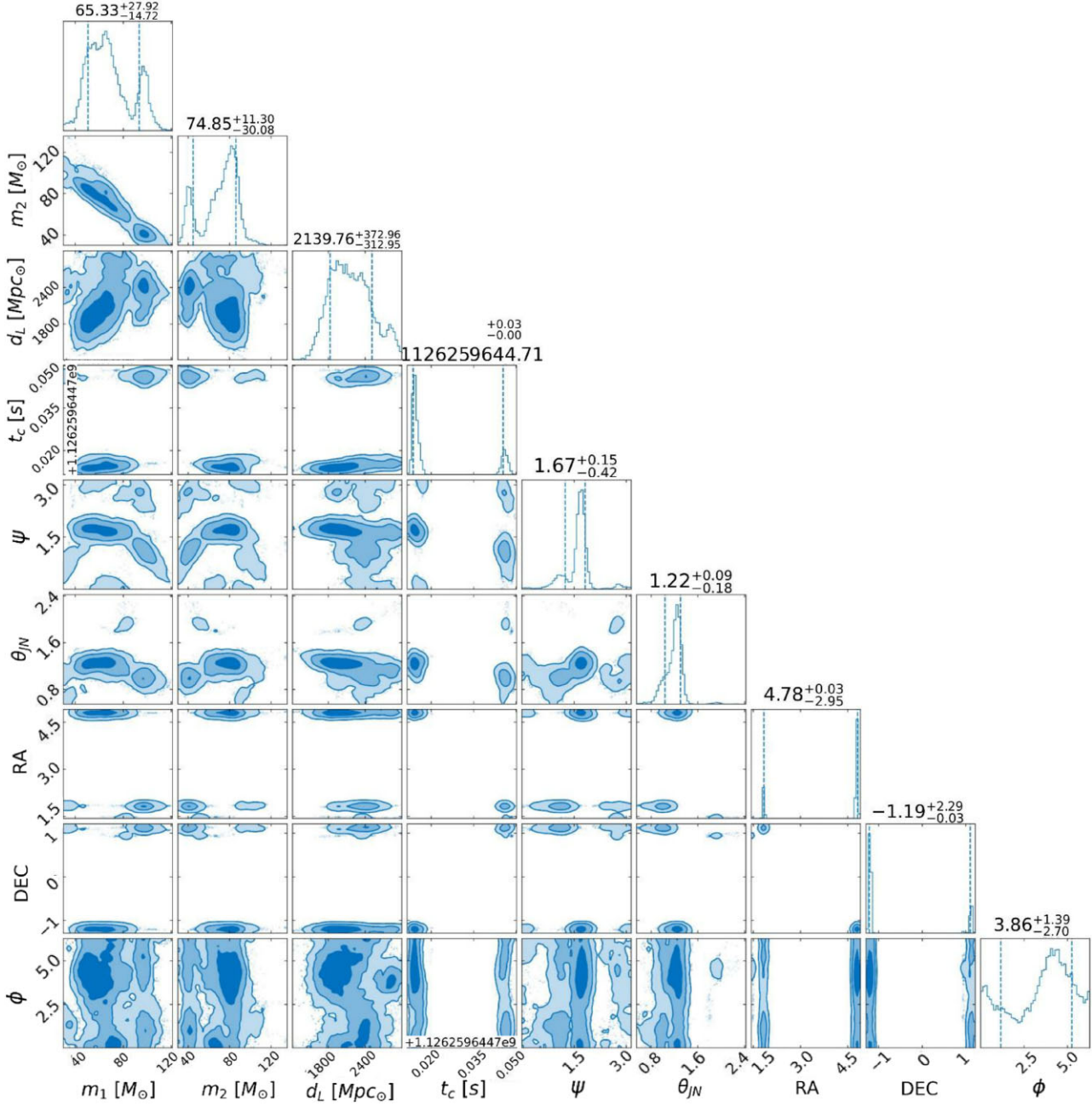
Figure A4. The posterior probability density distribution for a parabolic BH capture, recovered using a spinning BBH model and the DYNESTY sampler. Here, we show the posterior for the main parameters and omit six spins.

This paper has been typeset from a TEX/LATEX file prepared by the author.